Egypt. J. Chem. **Vol. 65,** No. 10 pp. 171 - 182 (2022)

Egyptian Journal of Chemistry

http://ejchem.journals.ekb.eg/

Synthesis, Structural and Electrochemical Performance of Tetragonal Spinel $MgMn_2O_4$ Cathode Materials Promoted by 3d and 4 d Transition Element

N.M. Yousif[a]*, M.R. Balboul[b]

[a]*Electrochemical Lab., and Thermal Analysis Lab., Solid-State and Accelerators department, National Center for Radiation Research and Technology (NCRRT), Egyptian Atomic Energy Authority (EAEA) B.O. Box 29 Nasr City, Cairo, Egypt*

[b]*Solid State Physics and Accelerators Department, National Centre for Radiation Research and Technology (NCRRT), Egyptian Atomic Energy Authority (EAEA), B.O. Box 29 Nasr City, Cairo, Egypt*

Abstract

Mg-ion batteries are rechargeable aqueous metal-ion batteries (RAMBs) and eco-friendly energy storage devices. Herein, we have fabricated T-$MgMn_2O_4$, and T- $MgNd_{0.02}Co_{0.18}Mn_{1.78}O_4$ spinel cathode materials via modifying the sol-gel route. This eco-friendly modified method is low cost, high stability, and low toxicity which is carried out by gamma radiation in the Co^{60} gamma cell source with a dose rate of 1.2 kGy/h. This method presented good advantages such as lower temperature compared to the solid-state reactions, better homogeneity, improved reactivity, and new compositions, and better control of stoichiometry, particle size, and purity. The structure and morphology of the as-prepared materials were investigated by X-ray diffraction (XRD), electron spin resonance (ESR), Raman, and scanning electron microscope (SEM). The electrochemical properties of the as-prepared materials were discussed. Finally, the charge-transfer resistance (R_{ct}), and the discharge specific capacity at current density 1mA/g for T-$MgMn_2O_4$ and T- $MgNd_{0.02}Co_{0.18}Mn_{1.78}O_4$ were 369.8 Ω, 299 mAh/g, and 196.7 Ω, 209 respectively. The capacity fading is reduced by doping with a small concentration of (Nd, and Co) as compared to the pure $MgMn_2O_4$ cathodes; construction is suitable for Mg-ion battery applications. A small quantity of rare earth metal elements could improve the stability of the Tetragonal Spinel $MgMn_2O_4$ Cathode Material. Moreover, the improvement of the electrochemical performance of the prepared cathodes nanocomposite by gamma-irradiated arises from the enlargement of the effective electrochemical area along with the enhancement of electrochemical impedance.

Keywords: Rechargeable Aqueous Mg-ion Batteries; Tetragonal-Spinel Cathode Materials; Modified Sol-gel route; XRD; Raman spectroscopy; Electrochemical Properties

1. Introduction

Renewable energy plays a vital role in our lives as energy, in general, is the basis for human survival [1]. The electrochemical energy storage devices and secondary metal ion batteries can be used for renewable energy effectively [2]. Environmental Economics and Energy (EEE) recommends using multivalent-metal ion storage batteries (i.e. Mg^{2+}, Zn^{2+}, and Al^{3+} Batteries) rather than Lithium-Ion Batteries (LIB's), due to having large efficient electrical energy storage systems [3], high level of safety in electrolytes [4]. Non-lithium battery systems (such as sodium-ion and metal-air batteries and Rechargeable Mg batteries) are presently used for future applications as in hybrid electric vehicles (HEV) or electric vehicles (EV), and portable electronic (laptops and smartphones)[5]. Magnesium Batteries have led us to take a radically different approach [6]. However, alkaline earth metals, similar passivation films tend to be formed through which cations diffuse slowly or not at the base [7]. Mg is the fourth most common element on earth (next to iron, oxygen, and silicon), and it is the third most abundant element dissolved in seawater [8]. Also, Mg is a light, abundance in the earth's crust, environmentally friendly, non-toxic, bivalent t, and relatively cheap metal whose high negative reduction potential is -2.356 V (vs. SHE), and its, high specific volumetric potential capacity is ca. 2200 mAh g^{-1} (3833 mAh cm^3)[8]. Therefore, Magnesium is based on secondary batteries. Rechargeable Mg-ion batteries have numerous challenges such as the development

*Corresponding author e-mail: yousif_nashwa@yahoo.com.; (N.M. Yousif).
Receive Date: 23 December 2021, Revise Date: 14 February 2022, Accept Date: 22 February 2022
DOI: 10.21608/EJCHEM.2022.112719.5116
©2022 National Information and Documentation Center (NIDOC)

of anodically stable, ion-conducting electrolyte solutions, good stability of electrolytes without lack, low kinetics of slow magnesium-ion diffusion into electrodes [9]. Moreover, the secondary rechargeable Mg-ion batteries have another advantage such as the evolution of the passivation layer, low specific energy, and high operating voltages of positive electrode hosts (cathode) without reducing in power[10]. Moreover, rechargeable multivalent-metal ion storage batteries (such as Mg^{2+}, Ca^{2+}, and Zn^{2+}) are novel to replace Li^{+} because of double the amount of charge stored per intercalated ion. In general, a metal-ion battery cell consists of an anode, electrolyte, and cathode; the anode in plate metal form permits energy gains in energy storage. However, the novel cathode material (or positive electrode material) must have good structural stability to improve the power and energy density, cell capacity, and battery life cycle [11]. The materials that are typically used for fabricating the anode are metallic Magnesium, graphitic carbon, hard carbon, synthetic graphite, Magnesium titanate, tin-based alloys, and silicon-based materials. The materials used for making cathode are an oxide of Magnesium manganese, Magnesium cobalt oxide, FeS_2, V_2O_5, Magnesium nickel, cobalt manganese oxide, Magnesium ion phosphate, and electronic conducting polymers .The materials used as electrolytes include organic and aqueous solutions .Apart from these main components, there are other components such as a binder, flame retardant, gel precursor and electrolyte solvent [12]. Because of the safety concerns and high cost, spinel $MgMn_2O_4$ and olivine $MgFePO_4$ have become appealing for transportation applications due to the low cost and environmental courtesy of Mn and Fe, good structural and chemical stabilities, and high charge-discharge rate capability. However, their limited energy is a drawback. Mn dissolution due to the disproportionation of Mn^{3+} into Mn^{4+} and Mn^{2+} is the major issue that has plagued spinel $MgMn_2O_4$ over the years [13]. The spinel crystal structure is recognized and promising as a positive electrode (cathode) material in the battery market, especially its relatively cheap, high operating voltage and good kinetics, three-dimensional (3D) pathway. Additionally, the spinel crystal structure is considered novel cathode structure material due to its safe, rapid diffusion of ions, environmentally benign, and structural stability [13]. The spinel Mg Mn2O4 cathode material has a cubic or tetragonal structure based on the preparation temperature and doping. The tetragonal phase (T- Mg Mn_2O_4) structure is a promising cathode material, due to high theoretical capacity (~ 272 mAh g^{-1}), high mobility of Mg $^{2+}$ cation in an electrolyte, the existence of high spin Mn^{3+} ion in $MgMn_2O_4$ leading to the Jahn-Teller effect [14].Therefore, this paper aims to novel synthesized by using gamma irradiation to obtain a gel product instead of heat treatment for tetragonal-spinel cathode electrodes. We report a simple synthesis method that we employed to design and fabricate tetragonal-spinel (T-$MgMn_2O_4$) and (T-$MgNd_{0.02}Co_{0.18}Mn_{1.78}O_4$) via a modified sol-gel route [15] by using metal acetates as the raw materials and citric acid as the complexing agent. The structural and morphology of tetragonal-spinel cathode materials are explored by XRD, ESR, Raman, and SEM. We also considered the electrochemical properties and mechanisms of the reactions in an aqueous electrolyte at a 0.5 mV/s potential scan rate in the potential range (from -0.8 to 1.2 V). Finally, specific capacity, electrochemical impedance (EIS), and its equivalent circuit have been determined.

2. Materials and Methodology

2.1. Materials

All chemicals used in this study are of high purity such as Magnesium Acetate Tetrahydrate ($(CH_3.COO)_2$. $Mg.4H_2O$, Mw = 214.45, LOBA Chemie, 98%), Manganese II Acetate Tetrahydrate ($(CH_3COO)_2$ $Mn.4H_2O$, Mw = 245.09, LOBA Chemie, 98.5%), Cobalt Acetate ($(CH_3COO)_2Co.4H_2O$, Mw = 249.08, Nice Chemicals Pvt. Ltd) and Neodymium III Nitrate Hexahydrate ($Nd(NO_3)_3.6H_2O$, Mw = 438.34, LABORT FINE CHEM Pvt. Ltd) precursors. Citric Acid E.P. Monohydrate ($C_6H_8O_7.H_2O$, Alpha Chemika) was used as a chelating agent.

3.2. Synthesis of tetragonal spinel cathode materials

A stoichiometric amount of magnesium acetate and manganese acetate with the molar ratio of (Mg+: Mn+=1:2) were dissolved in double distilled deionized (DI) water as the solvent with constant stirring. The molar fractions of citric acid: total metal ions=1:1; WMR (32%) from the ammonium solution was operated to regulate the sol-gel solution pH to 7. The required amount of citric acid was added to the above mixed with a stirring speed of 250 rpm and a temperature of 80 °C. Full gel structures were formed

after the mixture was poured into sealed glass bottles and exposed to a total gamma radiation dose of 25 kGy at a dose rate is approximately 1.2 kGy/ h. The scheme for preparation is shown in figure1. The irradiation process was conducted on the 60Co facility of National Center for Radiation Research and Technology (NCRRT), (made in Russia) Egyptian Atomic Energy Authority, Cairo, Egypt. Achieved gels were dried at 120 °C for 12 hours in a hot air oven to evaporate water from the gel. Then the calcination processes were carried out at 300 °C for 6 hours, the resultant pioneer was grounded using mortar and pestle. Finally, the calcined powdered was subjected to heat-treatment in a muffle furnace at 800, 850, 800 °C for 6, 8, 12 hours, respectively, and a heating rate of 1 °C/min to get the final black color product $MgMn_2O_4$ (T-MMO) and $MgNd_{0.02}Co_{0.18}Mn_{1.78}O_4$ (T-MNCMO).

We have chosen this novel method for many reasons as mentioned below: first, this field (gamma or electron beam) is used in many peaceful areas such as:

A- Preparation materials (like modified sol-gel method, Polymerization for several polymers)

B- Effect of radiation on the structure and some properties of some materials,

C- Crosslinking for co-polymers (like LDPE and HDPE, etc..)

D- Reduction for several materials (like silver nitrate to obtain Ag Np, reduction for graphene oxide to obtain r GO, etc..).Second, this method of preparation is environmentally friendly, low cost, high stability, and has low toxicity over large-scale commercial applications. Finally, the resulting materials from our novel gamma irradiation gelation step in preparation have a large surface area and high homogeneity. This method presented good advantages such as lower temperature compared to the solid-state reactions, better homogeneity, improved reactivity, and new compositions, and better control of stoichiometry, particle size, and purity. Therefore, this novel method has opened new directions for molecular architecture in the synthesis of perovskites.

3. Material Characterizations

The crystal structural analysis was carried out using X-ray diffraction (XRD) in a Shimadzu -2000 instrument with Cu Kα radiation (λ = 1.5406A°) as the source at 40 kV and 10°/min scanning rate between 2θ =4°-90° diffraction angle. The morphology of the products was investigated using a JEOL-T20, scanning electron microscope (SEM). The vibrational modes of molecules were determined using Raman spectroscopy by Jobin–Yvon model U1000, between 4 and 1200 cm-1 at room temperature, a double monochromatic has been used with argon-ion laser line radiation used as a source of light, which has wavelength ~ 514.5 nm and using a low excitation power of 10 mW. The free radicals created (ESR signals) were detected at room temperature by an X-band EMX spectrometer (Bruker, Germany) using a standard rectangular cavity of ER 4102. All experiments are carried out at room temperature (23℃).

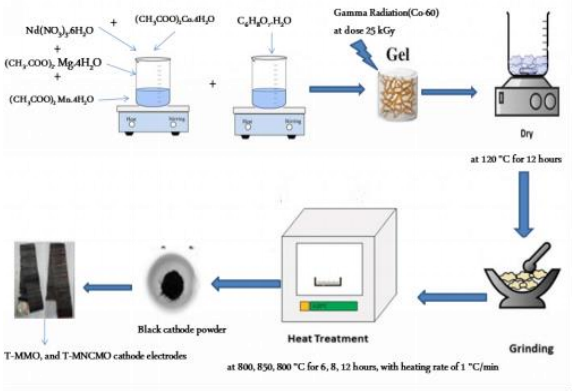

Figure 1 the synthesis of T-MMO and T-MNCMO by the modified the sol-gel route

3.3. Cathode electrode fabrication and electrochemical measurements

To make the electrodes for electrochemical studies, the working electrodes were fabricated via a combination of active material (T-$MgMn_2O_4$) and (T-$MgNd_{0.02}Co_{0.18}Mn_{1.78}O_4$) with conductive carbon black or acetylene black (graphite) and polyvinylidene fluoride (PVDF) as a binder with a weight ratio of 80:10:10, respectively. Subsequently, mixed smoothly dissolve in NMP with stirred vigorously for 6 h to form a slurry. The overhead mixture of 15 µm was pipetted gradually and drop-casted coated onto pre-cleaned Al paper (2.02.0 cm^2); coating thickness was adjusted to ≈ 300 µm. The coated electrode was dried at 100 ℃ for 24 hrs under a vacuum oven to remove the remaining solvent.

Electrochemical analysis for the above-prepared working electrodes was tested in a three electrodes cell with 1M of magnesium sulfate dissolved in water ($MgSO_4$ aqueous solution) as the electrolyte, the Pt-wire as a counter electrode, the Ag/Ag Cl as a reference electrode. Electrochemical measurements

were carried out using a Biologic SP-300 analyzer German electrochemical workstation. Biologic EC-lab analytical with attached galvanostat/ potentiostat/ EIS modules was used for cyclic voltammetry (CV) and galvanostatic charge/discharge (GCD) and electrochemical impedance spectroscopy (EIS) measurements. Cyclic voltammetry (CV) was carried out at a scan rate of 0.5 mV/ s with a voltage window of (from -0.8 to 1.2 V), and at different scan rates (200, 150, 100, 70,50,30,10 mV/ s); the galvanostatic charge-discharge (GCD) studies were done for a current density of 10 mA g^{-1} for a voltage range of (0 - 1 V). Electrochemical Impedance Spectroscopy (EIS) study was recorded with frequencies ranging from 100 mHz to 200 kHz at an ac amplitude voltage of 10mV. These electrochemical investigations were carried out at room temperature (23℃).

4. Results and Discussion

4.1. Structure, morphology analysis of the as-prepared nanocomposites

4.1.1. XRD analysis

The X-ray diffraction patterns of $MgMn_2O_4$ and $MgNd_{0.02}Co_{0.18}Mn_{1.78}O_4$ are shown in Figure 2. Every one of the diffraction features was indexed to the tetragonal crystal structure, which fitted by the "Fityk1.3.1 program" albeit with a small secondary phase. The patterns show that the tetragonal spinel structure has been profitably achieved for the prepared nanocomposites with a space group of I41/amd (141), cell parameters (a=b=5.727 Å, and c=9.284 Å), cell volume 304.5 Å3, and the calculated density is 4.322 g/cm3 in agreement with ICSD (no. 00-072-1336)by using a software "POWD MULT"[16]. The main 2θ values at 18°, 29o, 32°, 36o, 38o, 44o, and 60° can be indexed as (101), (112), (103), (211), (004), (220), and (224) respectively, reflections of (T-$MgMn_2O_4$); which is in good agreement with the informed results in[17]. The structure of T-$MgMn_2O_4$ is arranged at interconnected chains of edge-sharing MnO_6 octahedral, cross-linked by corner-sharing single MgO_4 tetrahedral [18]. A cation migration is detected in T-$MgMn_2O_4$, in which Mg^{2+} and Mn^{3+} exchange positions due to their comparable ionic radii (0.63 Å for tetrahedral Mg^{2+} and 0.72 for octahedral Mn^{3+}, respectively)[19]. Thus, The Jahn-Teller effect of Mn^{3+} in spinel magnesium manganese oxide ($MgMn_2O_4$) has been prompted a tetragonal structure. The site inversion understands the disproportionation reaction obtained below in Kröger–Vink symbolization:

$$Mg\times_{Mg}(Tet) + 2Mn\times_{Mn}(Oct) \rightarrow Mn\bullet_{Mg}(Tet) + Mg'_{Mn}(Oct) + Mn\times_{Mn}(Oct)$$

The small concentration from Co and Nd doping has no influence on the crystal structure of the host T-$MgMn_2O_4$ material, but some peaks shift on the way to higher angles, and smaller lattice parameters. Also, we can calculate the crystallite size (D) and the microstrain (ε) of the nanocomposites using the following relation [20]:

$$\beta \cos\theta / \lambda = k / D + 4\varepsilon \sin\theta / \lambda \qquad 1$$

where λ is the wavelength of incident radiation, k is a dimensionless shape factor that assumes a typical value of ~0.9, and β is the full width at half maximum (FWHM) of the diffraction peaks. The amount of strain is given by the slope of the straight line, while the crystallite size is given by the intercept on the β cosθ/λ axis. Moreover, the specific surface area (S) of the T- $MgMn_2O_4$ nanostructures prepared can be calculated by using the relation given below [21]:

$$S = 6*10^3 / D\, d_x \qquad 2$$

where d_x is the X-ray density and D is the crystallite sizes. The calculated crystal structure parameters crystallite sizes, microstrain, and specific surface area are reported in Table 1. It is clear from the calculation that a crystal size of less than 100 nm has been reached. This provides shorten transport lengths for the electrons in the matrix, which also promotes cation mobility in the electrolyte. Moreover, the small concentration from Co and Nd doping increases the surface area of the cathode electrode material which is an important feature for the energy and power density in the metal ion-battery system [22].

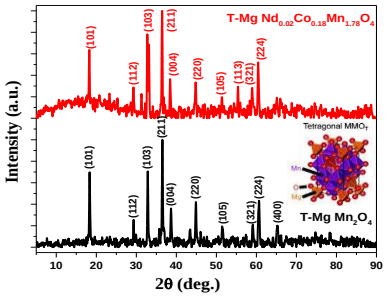

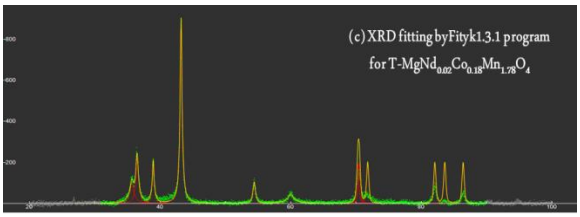

Figure 2(a) The X-ray diffraction patterns of T-$MgMn_2O_4$ and T$MgNd_{0.02}Co_{0.18}Mn_{1.78}O_4$, spinel structure (inset figure), and (c) XRD fitting byFityk1.3.1 program for T-$MgNd_{0.02}Co_{0.18}Mn_{1.78}O_4$.

Table 1 the values of crystallite sizes, microstrain, and specific surface area for T-$MgMn_2O_4$, and T- $MgNd_{0.02}Co_{0.18}Mn_{1.78}O_4$cathode material samples

Sample	Crystalline size, D (nm)	Strain	Specific surface area, S (m^2/g)
T-$MgMn_2O_4$	47.36	1.26×10^{-3}	29.3
T-$MgNd_{0.02}Co_{0.18}Mn_{1.78}O_4$	84.9	7.37×10^{-4}	16.35

4.1.2. Morphology Study

The morphology was studied using a scanning electron microscope (SEM). Figure 3 shows the formation of crystalline $MgMn_2O_4$ and $MgNd_{0.02}Co_{0.18}Mn_{1.78}O_4$ spinel samples. Slight changes in porosity due to calcination appear on the surface of the prepared samples. The calcination temperature was over 800 ° C which could be responsible for creating holes and pores which are caused by a large amount of gases emitted through the prepared process [23]. Also, it easily indicates the development of the clusters and fragile network structure, because the cathode material samples were prepared by the sol-gel technique. The bulk of the crystal shows the diamond configuration of the spinel framework however, the surface exhibits a diamond configuration with visible contrast at the center octahedral sites and the absence of contrast at the tetrahedral sites. Contrasting particles of $MgMn_2O_4$ possessing octahedral shapes with sharp edges and flush surfaces, particles of $MgNd_{0.02}Co_{0.18}Mn_{1.78}O_4$ have a more skirted shape with grooved surfaces. With the lowest Nd content, the particle still possesses some characteristics of octahedral shape but tends to grow into a rounded shape [24].

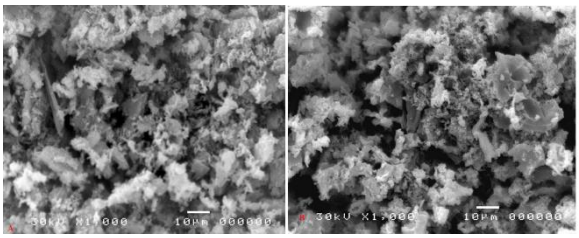

Figure 3 the scanning electron microscope (SEM) of (a) T- $MgMn_2O_4$, and (b) T-$MgNd_{0.02}Co_{0.18}Mn_{1.78}O_4$ spinel samples

4.2. Vibrational analysis of the as-prepared nanocomposites

4.2.1. Raman Spectra analysis

Raman spectrum of T-$MgMn_2O_4$ and T-$MgNd_{0.02}Co_{0.18}Mn_{1.78}O_4$ spinel samples in the wavenumber range from 200 to 1000 cm^{-1} is illustrated in Figure 4. The tetragonally disfigured spinel of $MgMn_2O_4$ oxides is dominated by the Mg ions in the locations of the tetrahedral plan. The stationary collaborative Jahn–Teller distortion is for Mn^{3+} ions in the octahedral positions as a result of the tetragonal elongation of the two apical Mn–O bonds. On the other hand, the crystal structure of $MgMn_2O_4$ spinel at a calcination temperature above 600 belongs to the I41/adm space group. Also, the Factor group analysis can be achieved with the assistance of the correlation technique [25], which provides 10 allowed Raman phonon modes with ($\Gamma = 2A_{1g}+3B_{1g}+B_{2g}+4E_g$). Generally, spinel manganese oxides materials have energies in the range of ~ 600–650 cm-1 which attribute vibrations relating to the motion of oxygen exclusive to the octahedral unit MnO_6. Particularly in $MgMn_2O_4$ spinel, peak 1 is the strongest one in the phonon mode at 661.05 cm^{-1} for Mn_3O_4 which belongs to A_{1g} symmetry[26]. Also, it is remarked that a distinct broad peak 2 is located nearby 514.98 cm^{-1} and has a low intensity for all spectra. Moreover, Peak 2 belongs to B_{2g} mode and outcomes permit the direct function of the tetrahedral cation in this ordinary mode ascription. Besides at inferior energies, peak 3 has been investigated at 378.3 cm^{-1} which signifies E_g (1) model in which the irregular shape of Mn_3O_4 anticipated the occurrence of a complementary element. Peak 4 denotes Mn_3O_4 at 312.66 cm^{-1} which belongs to B_{1g} (1) and its intensity diminishes in $MgMn_2O_4$, which has a minor intensity for all spectra[25]. Correspondingly, it appears that this peak is exactly influenced by the Mg ion, including reinforcement and a good correlation by reducing ionic radii, which may be originated

between the peak energy and the Mg–O bond lengths[12].

The extra Raman mode was at an elevated frequency and modified loosely in parallel with the A_{1g} essential mode in the entire composition. This characteristic opposes the ascription of the extra Raman line to a vibration mode of the impurity phase. This electronic feature is similarly dependable for a baseline that is not smooth and can be denoted by a very broad peak. The fitting spectra were approved; this investigation structure is expected to be of the Lorentzian formula and the baseline was being supplemented in a small range of wavenumbers in the range 200 - 250 cm^{-1} since only this 'wing' of the Rayleigh peak, is distinguished in our trials.

There are no differences in the Raman spectra of the ordered spinel structure and the 3-D distribution of phases in doping $MgMn_2O_4$ spinel material with Co and Nd elements. But, there are changes in the intensity of vibrational peaks which due to the doping effect[14]. However, the shift in wavenumber to lower sides occurred in A_{1g} and B_{2g} modes, and also the FWHM was increased. The main reason for these lower shifts in wavenumbers is the increase in the effective mass of the Mn(Nd)-O bond due to the larger atomic weight of Nd than Mn. Furthermore, the increase in FWHM is due to the disorder at the site of the oxygen octahedral[27]. The Raman parameters such as vibrational modes, FWHM, height, and area are tabulated in table 2.

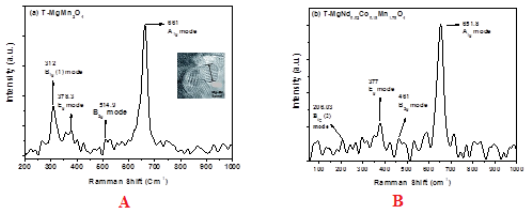

Figure 4 Raman spectrum of (a) T-$MgMn_2O_4$ and diffraction pattern (inset figure), and (b) T-$MgNd_{0.02}Co_{0.18}Mn_{1.78}O_4$ spinel samples

Table 2 the values of Raman vibrational modes, FWHM, height, and area for T-MMO, and T-MNCMO cathode material samples obtained by Nelder-Mead simplex fitting method using Fityk program

Samples	Vibrational modes	Peak Position (cm^{-1})	Height	Area	FWHM
T-$MgMn_2O_4$	A_{1g}	661	17.9	1112.4	39.5
	B_{2g}	514.9	9.04	207.7	24.6
	E_g	378.3	7.05	356.4	14
	B_{1g} (1)	312	5.6	110.4	12.5
T-$MgNd_{0.02}Co_{0.18}Mn_{1.78}O_4$	A_{1g}	651.8	26.08	2267.1	55.3
	B_{2g}	461	5.6	189.9	33.5
	E_g	377	12	171.2	15.4
	B_{1g} (1)	295	9.5	112.2	12.8

4.2.2. Electron Spin Resonance (ESR) analysis

ESR spectroscopy was used to detect unpaired electrons (free radicals) in the prepared samples and to analyze paramagnetic species. The ESR spectra for T-MMO and T-MNCMO cathode material samples are shown in Figure 5. A quantitative ESR analysis of magnesium-manganese spinel phase was created by Lorentzian function method. In general, Mn^{2+} (total spin S = 5/2) and Mn4+ (S = 3/2) and (μ = 3.87 μ_B) are paramagnetic species, and hence ESR-active, while diamagnetic Mn^{3+} (S = 2) is not active and so "silent" in electron spin resonance (ESR). From Figure (5a) it can be noticed that direct tetragonal spinel signals credited to Mn 3+ ions have non the Jahn–Teller effect (JTE), while, Mg^{2+} ions are on the octahedral sites and Mn^{3+} ions on the tetrahedral ones. This can be attributed to the charge balance presence or an equal number of Mn ions on octahedral sites. In other words, the ESR signals are either decreased in intensity or inactive due to the very low tetragonal distortion of the related Mn $^{3+}$ octahedral distortion.

From Figure (5b) in it can be observed that the ESR spectrum has paramagnetic behavior and the lone pair of electron states is identified due to a small value of the magnetic moment supported by Mn^{4+} ions which are compared with expected for a spin S = 3/2. However, the sharp signal position for uncorrelated spins Mn^{4+}–Mn^{4+} is dipolar interactions. But, the obtained broadening signal of Mn^{4+}–Mn^{3+} is correlated due to the charge state of the manganese localizes and the electronic structure of prepared cathode material samples [28] which is confirmed by the Raman spectra of our samples. From the Lorentzian line based on the Zeeman Effect, The g value can be determined. The fitting procedures are peak center, linewidth or full width at half maximum (FWHM), peak height, $g_{\parallel}$, $g_{\perp}$ values, and the number of spins are about 3473.1 G, 44.8, 19608 G, 1.99405, 2.00988, and 2.07058 1020 respectively for T-$MgNd_{0.02}Co_{0.18}Mn_{1.78}O_4$ cathode material sample. The obtained results from ESR analysis about the

electronic structure of T-MMO and T-MNCMO cathode material compounds are confirmed by the Raman spectra analysis. Finally, ESR technique proved that T-$MgMn_2O_4$ and T-$MgNd_{0.02}Co_{0.18}Mn_{1.78}O_4$ compounds are promising as cathode materials, and also, as high-voltage spinel-type materials for magnesium-ion battery [29].

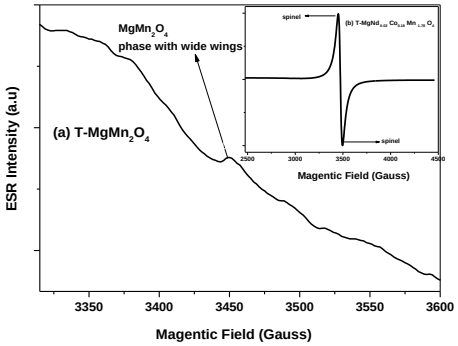

Figure 5 the ESR spectra for (a) T- $MgMn_2O_4$, and (b) T$MgNd_{0.02}Co_{0.18}Mn_{1.78}O_4$cathode material samples

4.3. Electrochemical properties of the as-prepared nanocomposites cathode

4.3.1. Electrochemical Impedance Spectroscopic(EIS) analysis

EIS is an important tool to study the impedance that occurs during the intercalation /de-intercalation of Mg^{2+} ion during the redox process, as well as the electrical properties of the cathode material for metal-ion battery [30]. The Nyquist plot of T-$MgMn_2O_4$ and T-$MgNd_{0.02}Co_{0.18}Mn_{1.78}O_4$ compounds is shown in figure 6. From the figure it is clear to see two distinct regions: (a) semicircular arc (the ionic conductivity) in the high-frequency region and (b) straight line (the electronic conductivity) in the low-frequency region. The diameter of the semi-circle has reflected the value of the charge-transfer resistance (R_{ct}), which is associated with the formation of a passivation film on the surface of the cathode materials [31]. Besides, the linear portion in the low-frequency region is designated to Warburg impedance (W), which is ascribed to the diffusion of Mg ions into the bulk of the electrode materials. The calculated parameters of electrochemical impedance spectra based on the equivalent circuit are tabulated in Table 3. The resistance of solution (R_S) and the resistance of electrolyte interface (R_{SEI}) are potential-independent and have small differences due to the stability between the electrolyte and the surface electrodes. Battery discharging with a higher current value is due to diminishing the charge transfer resistance (R_{ct}), whereas the capacity fades during cycling due to the increase in the charge-transfer resistance (R_{ct}) value [18],[32]. The electrical properties of cathode materials are ascribed by the Bode plot. The Bode plot is the plot between (log frequency) and (log Z) of T-$MgMn_2O_4$ and T-$MgNd_{0.02}Co_{0.18}Mn_{1.78}O_4$ compounds as shown in figure 7a. The relationship between phase Z and the frequency of T-$MgMn_2O_4$ and T-$MgNd_{0.02}Co_{0.18}Mn_{1.78}O_4$ compounds is shown in figure 7b. This figure indicates the stability and efficiency of the cathode materials for Mg-ion battery.

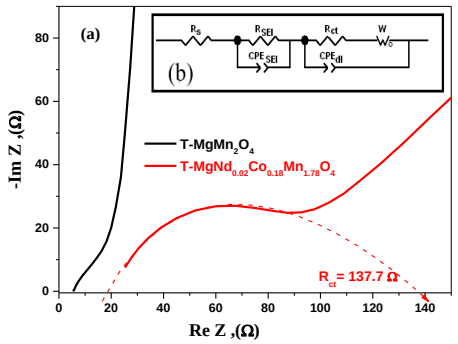

Figure 6 the Nyquist plot of (a) T-$MgMn_2O_4$ and T-$MgNd_{0.02}Co_{0.18}Mn_{1.78}O_4$ compounds, and (b) equivalent circuit of cathode material samples

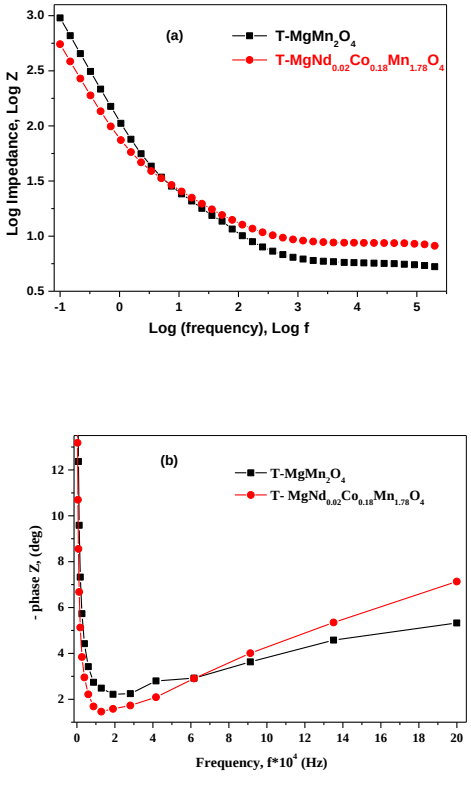

Figure 7(a) the Bode plot of T-$MgMn_2O_4$ and T-$MgNd_{0.02}Co_{0.18}Mn_{1.78}O_4$ compounds, and (b) the relationship between phase Z and frequency of T-$MgMn_2O_4$ and T-$MgNd_{0.02}Co_{0.18}Mn_{1.78}O_4$ compounds

Table 3 The calculated parameters for electrochemical impedance such as the charge-transfer resistance (R_{ct}), Warburg impedance (W), The resistance of solution (R_S), the resistance of solid electrolyte interface (R_{SEI}), capacitance of solid electrolyte interface, and double-layer capacitance of electrochemical impedance spectra based on the equivalent circuit.

Samples	R_{ct} , Ω	W, $\Omega.s^{-1/2}$	R_s, Ω	R_{SEI}, Ω	CPE_{SEI}, F.s/A	CPE_{dl}, F.s/A
T-$MgMn_2O_4$	369.8	1.059	5.64	0.69	5.17×10^{-12}	1.054×10^{-3}
T-$MgNd_{0.02}Co_{0.18}Mn_{1.78}O_4$	137.7	119.9	0.022	8.38	2.23×10^{-7}	4.41×10^{-3}

4.3.2. Cyclic Voltammetry and cycling stability Studies of T-$MgMn_2O_4$ and T-$MgNd_{0.02}Co_{0.18}Mn_{1.78}O_4$ cathode materials in aqueous solution

In order to investigate the charge-discharge process, we performed a cyclic voltammetry test for the two as-synthesized cathode materials using a three-electrodes test cell in an aqueous electrolyte solution (1 M $MgSO_4$), the test voltage window was (-1 to 1 V) and at different scan rates (200, 150, 100, 70, 50, 30, 10 mV/s) as shown in Figures 8. It can be seen that the anodic current peak position is slightly shifted to a higher value of current with an increase in the scan rate due to electrode polarization, and the conductivity of the electrode materials, which indicates that the electrochemical kinetics of the electrode material has been greatly improved [33]. Using a very low scan rate at 0.5 m V/s a cyclic voltammetry experiment was performed and the CV plot of T-$MgMn_2O_4$ and T-$MgNd_{0.02}Co_{0.18}Mn_{1.78}O_4$ cathode materials is given in Figure 9. The low scan rate CV curve for T-$MgNd_{0.02}Co_{0.18}Mn_{1.78}O_4$ increases slightly in the peak current values compared to T-$MgMn_2O_4$, which indicates the periodic activation of the electrode material [33]. Doping with Co and Nd elements plays a critical role in the redox process because the rare-earth elements (e.g. La, Nd) stabilize the structure [34]. For the T-$MgMn_2O_4$ cathode material, two anodic small peaks (E_{pa}) are observed at (0.95, and 0.14V) and two cathodic peaks (E_{pc}) at (0.75, and -0.12 V). While for $MgNd_{0.02}Co_{0.18}Mn_{1.78}O_4$ cathode material, there are two broad anodic peaks (E_{pa}) at (1.13, and 0.12V) and one cathodic peak (E_{pc}) at (-0.23V) which is shifted to lower voltage after doing [35]. These redox peaks are noticed due to the stepwise co-intercalation of $Mn^{2+/}Mg^{2+}$ into the spinel for divalent intercalation in the manganese-based host for rechargeable aqueous metal-ion batteries (RAMBs)[36], [37]. The trend of CV plateau is indicated by the stable electrochemical reversibility of the cathode material and the electrochemical reactions during the discharge/charge process can be expressed by the following equations [30]:

$$MgMn_2O_4 \leftrightarrow Mg^{2+} + Mn_2O_4$$

The charge-discharge studies are carried out based on the best cyclic voltammetry results, the specific charge-discharge capacity against the potential of T-$MgMn_2O_4$, and T-$MgNd_{0.02}Co_{0.18}Mn_{1.78}O_4$ cathode materials is given in Figure 10. It can be seen that the highest discharge capacities are 299 mAh/g, and 209 mAh/g at a current density of 1 mA/g for T-$MgMn_2O_4$ and T-$MgNd_{0.02}Co_{0.18}Mn_{1.78}O_4$ cathode materials, respectively. The discharge capacity is in the reverse order for electrical conductivity. This is noticeably due to the reduction in active manganese ions in the case of doped compounds. The reduction in discharge capacity is due to the strong ionic interactions and the redistribution of the charged cation in the host material by doping [38]. The irreversibility of about 2% in the first cycle may be due to the formation of nanocomposite produced by gamma radiation into the fabricated electrodes increasing the available surface area with additional active sites for faradaic reactions, and fewer obstructions in the electron transfer process which indicates the remarkable electrochemical stability of this system. This demonstrates that the irradiated nanocomposites are well attached to the electrode surface and have not detached from the surface during the repeated charge-discharge process [39].

Cyclability is a phenomenon that reflects the specific capacity growth with increasing cycle numbers. The cycling stability is a momentous parameter for practical applications [40]. The cyclability pattern (the relationship between cycle number and capacitive retention (c_r %)) for T-$MgMn_2O_4$ and T-$MgNd_{0.02}Co_{0.18}Mn_{1.78}O_4$ cathode materials is given in Figure 11. It can be seen that T-$MgNd_{0.02}Co_{0.18}Mn_{1.78}O_4$ cathode material showed high reversible capacitive retention with nearly 99% and the coulombic coefficient was still high up to 99.8% after 50 cycles at a current of 1 mA/g; this is indicating to good cycling stability. This improvement in the cyclability is observed in T-$MgNd_{0.02}Co_{0.18}Mn_{1.78}O_4$ cathode materials due to the structural stability of Nd, and Co doping in T-$MgMn_2O_4$. It should be noted that this periodic activation process of the cathode electrode in an aqueous electrolyte is predominant during cycling because of the longer discharge/charge reaction time giving more reversible active sites, resulting in

increased specific capacity with increasing cycle numbers. Based on the earlier analysis, a significant improvement of the electrochemical performance of the prepared cathodes nanocomposite by gamma-irradiated arises from the enlargement of the effective electrochemical area along with the enhancement of electrochemical impedance. Second, the porous structure can offer enough space for ionic transport, and a shorter ionic diffusion path, prompting a good capability rate. In addition, the interconnected porous structure can offer more paths for the conduction of electrons, and the nanostructured surface exploits the transport of electrolytes and provides a wide surface area for charge-transfer reactions [41].

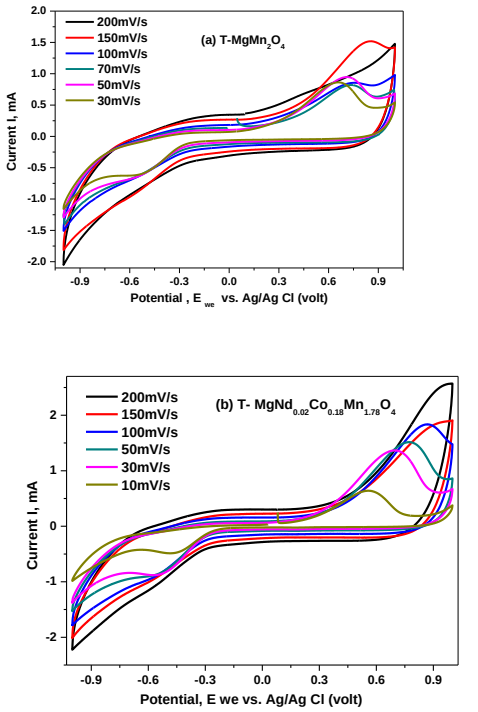

Figure 8 The cyclic voltammetry curves of (a) T-$MgMn_2O_4$, and (b)T-$MgNd_{0.02}Co_{0.18}Mn_{1.78}O_4$ cathode materials using a three-electrodes test cell in an aqueous electrolyte solution (1 M $MgSO_4$), the test voltage window was (-1 to 1 V) and at different scan rates (200, 150, 100, 70, 50, 30, 10 mV/s)

The relationship between charge time and power for T-$MgMn_2O_4$ and T-$MgNd_{0.02}Co_{0.18}Mn_{1.78}O_4$ is shown in Figure 12. The value of power in the case of Nd and Co-doped $MgMn_2O_4$ is lower than the case for $MgMn_2O_4$ at the same charge time. Nd^{4+} ions possess larger 4d electron orbitals than the 3d orbitals of Mn^{2+}, overlapping with O2- 2p orbitals may result in enhanced conductivity leading to enriched high evaluate performances of Nd and Co-doped $MgMn_2O_4$. However, the relationship between power and potential for T-$MgMn_2O_4$ and T-$MgNd_{0.02}Co_{0.18}Mn_{1.78}O_4$ is given in Figure 13. The value of power in the case of Nd and Co-doped $MgMn_2O_4$ is lower than the case for $MgMn_2O_4$ at the same applied voltage for charge and discharge time. A well-mannered rate capability for cathode materials is substantial in high power products such as EVs/HEVs meanwhile such apparatus regularly alterations between constant speed mode (moderate current output) and accelerating mode (large current output).

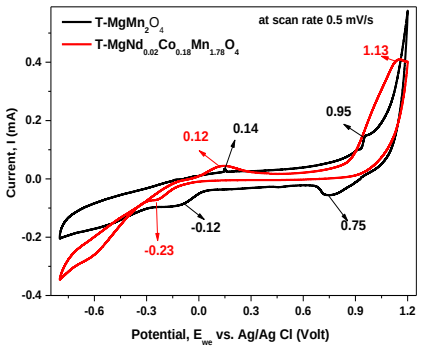

Figure 9 CV plots of T-$MgMn_2O_4$ and T-$MgNd_{0.02}Co_{0.18}Mn_{1.78}O_4$ cathode materials at very low scan rate at 0.5 m V/s

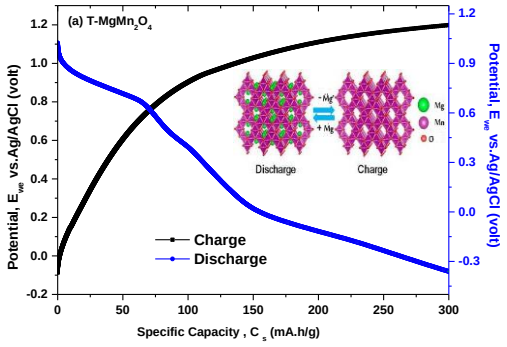

Figure 10 the specific charge-discharge capacity against the potential of (a) T-$MgMn_2O_4$, and (b) T-$MgNd_{0.02}Co_{0.18}Mn_{1.78}O_4$ cathode materials at a current density of 1 m A/g

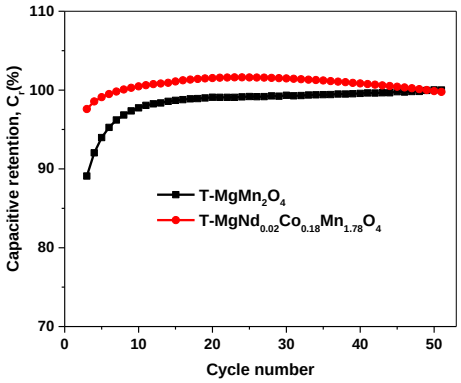

Figure 11 the cyclability pattern for T-$MgMn_2O_4$ and T-$MgNd_{0.02}Co_{0.18}Mn_{1.78}O_4$ cathode materials

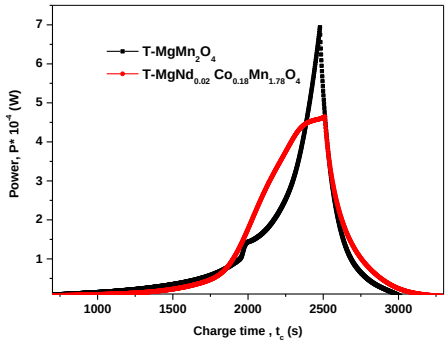

Figure 12 the relationship between charge time and power for T-$MgMn_2O_4$ and T-$MgNd_{0.02}Co_{0.18}Mn_{1.78}O_4$

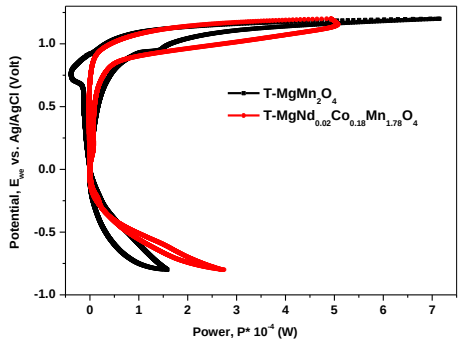

Figure 13 the relationship between power and potential for T-$MgMn_2O_4$ and T-$MgNd_{0.02}Co_{0.18}Mn_{1.78}O_4$

Conclusion

In the present paper, I am reporting, for the first time, the synthesis of T-$MgMn_2O_4$, and T-$MgNd_{0.02}Co_{0.18}Mn_{1.78}O_4$ spinel cathode materials by modified sol-gel route (citrate -gel method); Gelation step was carried out by gamma radiation in the Cobalt-60 gamma cell source (made in Russia) installed at the National Centre for Radiation Research and Technology, Cairo, Egypt (with dose rate 1.2 kGy/h). This method of preparation is environmentally friendly, low cost, high stability, and has low toxicity over large-scale commercial applications. I am also describing structural and electrochemical properties for prepared $MgMn_2O_4$ and Mg $Nd_{0.02}$ $Co_{0.18}$ $Mn_{1.78}$ O_4 cathode materials. The potential applications of these multifunctional cathode electrode materials were concluded as conformist substances in Mg-ion battery technologies. Especially in this article, the improvement of the specific capacity of this multifunctional cathode electrode material $MgMn_2O_4$ has been depicted by doping 3d transition elements like Co and small concentration from 4d rare earth elements like Nd. Doped 3d orbitals and 4d orbitals, radius overlapping with O 2p orbitals have been suggested to be major appliances for improved electronic conductivity. These results accessible have revealed the ability of 3d and 4d transition metals doping to develop high-rate electrochemical performances of spinel-structured $MgMn_2O_4$ cathode materials. Summing up the results, it can be concluded that, this approach may cover the technique for the workable application of spinel-structured transition metal oxides as cathode materials for the new generation of high-power Mg-ion batteries.

Acknowledgment

The authors gratefully acknowledge the generous experimental support of Egyptian Atomic Energy Authority (EAEA). This research was supported by National Centre for Radiation Research and Technology (NCRRT).

Funding

This research did not receive any specific grant from funding agencies in the public, commercial, or not-for-profit sectors. [No funding has been provided for this research].

Conflict of Interests

The authors declare that they have no known competing financial interests or personal relationships that could have appeared to influence the work reported in this paper

References

[1] M. M. Titirici et al., "Sustainable carbon materials," Chem. Soc. Rev., vol. 44, no. 1, pp. 250–290, 2015, DOI: 10.1039/c4cs00232f.

[2] W. Liu et al., "Nickel-Rich Layered Lithium Transition-Metal Oxide for High-Energy

Lithium-Ion Batteries," Angew. Chemie - Int. Ed., vol. 54, no. 15, pp. 4440–4457, 2015, DOI: 10.1002/anie.201409262.

[3] H. D. Yoo, I. Shterenberg, Y. Gofer, G. Gershinsky, N. Pour, and D. Aurbach, "Mg rechargeable batteries: An on-going challenge," Energy Environ. Sci., vol. 6, no. 8, pp. 2265–2279, 2013, DOI: 10.1039/c3ee40871j.

[4] P. Saha, M. K. Datta, O. I. Velikokhatnyi, A. Manivannan, D. Alman, and P. N. Kumta, "Rechargeable magnesium battery: Current status and key challenges for the future," Prog. Mater. Sci., vol. 66, pp. 1–86, 2014, DOI: 10.1016/j.pmatsci.2014.04.001.

[5] M. C. Lin et al., "An ultrafast rechargeable aluminum-ion battery," Nature, vol. 520, no. 7547, pp. 325–328, 2015, DOI: 10.1038/nature14340.

[6] A. Ponrouch, C. Frontera, F. Bardé, and M. R. Palacín, "Towards a calcium-based rechargeable battery," Nat. Mater., vol. 15, no. 2, pp. 169–172, 2016, DOI: 10.1038/nmat4462.

[7] J. Muldoon, C. B. Bucur, and T. Gregory, "Quest for nonaqueous multivalent secondary batteries: Magnesium and beyond," Chem. Rev., vol. 114, no. 23, pp. 11683–11720, 2014, DOI: 10.1021/cr500049y.

[8] H. Kim, G. Jeong, Y. U. Kim, J. H. Kim, C. M. Park, and H. J. Sohn, "Metallic anodes for next-generation secondary batteries," Chem. Soc. Rev., vol. 42, no. 23, pp. 9011–9034, 2013, DOI: 10.1039/c3cs60177c.

[9] E. Levi, M. D. Levi, O. Chasid, and D. Aurbach, "A review on the problems of the solid-state ions diffusion in cathodes for rechargeable Mg batteries," J. Electroceramics, vol. 22, no. 1–3, pp. 13–19, 2009, DOI: 10.1007/s10832-007-9370-5.

[10] I. Shterenberg, M. Salama, Y. Gofer, E. Levi, and D. Aurbach, "The challenge of developing rechargeable magnesium batteries," MRS Bull., vol. 39, no. 5, pp. 453–460, 2014, DOI: 10.1557/mrs.2014.61.

[11] P. Ram et al., "Synthesis and improved electrochemical performance of LiMn2 – xGdxO4 based cathodes," Solid State Ionics, vol. 300, pp. 18–25, 2017, DOI: 10.1016/j.ssi.2016.11.026.

[12] A. Mishra et al., "Electrode materials for lithium-ion batteries," Mater. Sci. Energy Technol., vol. 1, no. 2, pp. 182–187, 2018, DOI: 10.1016/j.mset.2018.08.001.

[13] A. Manthiram, "Materials challenges and opportunities of lithium-ion batteries," J. Phys. Chem. Lett., vol. 2, no. 3, pp. 176–184, 2011, DOI: 10.1021/jz1015422.

[14] A. Banu, A.Sakunthala, M. Thamilselvan, P. S. Kumar, K. Suresh, and S. Ashwini, "Preparation, characterization and comparative electrochemical studies of MgM X Mn 2-X O 4 (x=0, 0.5; M= Ni/Co)," Ceram. Int., vol. 45, no. 10, pp. 13072–13085, 2019, DOI: 10.1016/j.ceramint.2019.03.240.

[15] N. M. Yousif, N. Makram, and L. A. Wahab, "Structural, dielectric, and magnetic properties of LaCo0.2Mn0.8O3 and La2CoMnO6 perovskite materials," J. Sol-Gel Sci. Technol., 2021, DOI: 10.1007/s10971-021-05502-4.

[16] M. Cabello, R. Alcántara, F. Nacimiento, G. Ortiz, P. Lavela, and J. L. Tirado, "Electrochemical and chemical insertion/deinsertion of magnesium in spinel-type MgMn2O4 and lambda-MnO2 for both aqueous and non-aqueous magnesium-ion batteries," CrystEngComm, vol. 17, no. 45, pp. 8728–8735, 2015, DOI: 10.1039/c5ce01436k.

[17] J. Yin, A. B. Brady, E. S. Takeuchi, A. C. Marschilok, and K. J. Takeuchi, "Magnesium-ion battery-relevant electrochemistry of MgMn2O4: Crystallite size effects and the notable role of electrolyte water content," Chem. Commun., vol. 53, no. 26, pp. 3665–3668, 2017, DOI: 10.1039/c7cc00265c.

[18] Q. D. Truong et al., "Unravelling the Surface Structure of MgMn2O4 Cathode Materials for Rechargeable Magnesium-Ion Battery," Chem. Mater., vol. 29, no. 15, pp. 6245–6251, 2017, doi: 10.1021/acs.chemmater.7b01252.

[19] Q. D. Truong, H. Kobayashi, K. Nayuki, Y. Sasaki, and I. Honma, "Atomic-scale observation of phase transition of MgMn2O4 cubic spinel upon the charging in Mg-ion battery," Solid State Ionics, vol. 344, no. July 2019, p. 115136, 2020, DOI: 10.1016/j.ssi.2019.115136.

[20] G. K. Williamson and W. H. Hall, "X-Ray broadening from filed aluminum and tungsten," Acta Metall., vol. 1, pp. 22–31, 1953.

[21] P. Chand, S. Vaish, and P. Kumar, "Structural, optical and dielectric properties of transition metal (MFe2O4; M = Co, Ni, and Zn) nanoferrites," Phys. B Condens. Matter, vol. 524, no. July, pp. 53–63, 2017, DOI: 10.1016/j.physb.2017.08.060.

[22] P. Chand, V. Bansal, Sukriti, and V. Singh, "Effect of pH values on structural, optical, electrical and electrochemical properties of spinel LiMn2O4 cathode materials," J. Sci. Adv. Mater. Devices, vol. 4, no. 2, pp. 245–251, 2019, DOI: 10.1016/j.jsamd.2019.04.005.

[23] H.-M. Cho and Y. S. Meng, " Effect of Ni/Mn Ordering on Elementary Polarizations of LiNi 0.5 Mn 1.5 O 4 Spinel and Its Nanostructured Electrode," J. Electrochem. Soc., vol. 160, no. 9, pp. A1482–A1488, 2013, DOI: 10.1149/2.059309jes.

[24] W. Hailong, "4d Transition Metal Doped LiNi0.5Mn1.5O4 Cathodes for High Power Lithium Batteries," 2011.

[25] J. L. Dormann, A. Tomas, and M. Nogues, "Cation Ordering in LiFe5O8 Studied by Mössbauer Spectroscopy and X- Ray Crystallography," Phys. Status Solidi, vol. 77, no. 2, pp. 611–618, 1983, DOI: 10.1002/pssa.2210770225.

[26] B. Ammundsen, G. R. Burns, M. S. Islam, H. Kanoh, and J. Rozière, "Lattice dynamics and vibrational spectra of lithium manganese oxides: A computer simulation and spectroscopic study," J. Phys. Chem. B, vol. 103, no. 25, pp. 5175–5180, 1999, DOI: 10.1021/jp984398l.

[27] R. Singhal et al., "Synthesis and characterization of Nd-doped LiMn2O4 cathode for Li-ion rechargeable batteries," J. Power Sources, vol. 164, no. 2, pp. 857–861, 2007, DOI: 10.1016/j.jpowsour.2006.09.098.

[28] D. Capponi, M. Bini, G. Chiodelli, V. Massarotti, M. C. Mozzati, and C. B. Azzoni, "Structural transition in Mg-doped LiMn2O4: A comparison with other M-doped Li-Mn spinels," Solid State Commun., vol. 125, no. 3–4, pp. 179–183, 2003, doi: 10.1016/S0038-1098(02)00769-X.

[29] R. Sun et al., "Secondary-Phase Formation in Spinel-Type LiMn2O4-Cathode Materials for Lithium-Ion Batteries: Quantifying Trace Amounts of Li2MnO3 by Electron Paramagnetic Resonance Spectroscopy," Appl. Magn. Reson., vol. 49, no. 4, pp. 415–427, 2018, DOI: 10.1007/s00723-018-0983-4.

[30] F. Nobili, R. Tossici, R. Marassi, F. Croce, and B. Scrosati, "An AC impedance spectroscopic study of LixCoO2 at different temperatures," J. Phys. Chem. B, vol. 106, no. 15, pp. 3909–3915, 2002, DOI: 10.1021/jp013569a.

[31] Y. Ding, P. Zhang, and D. Gao, "Synthesis and electrochemical properties of layered Li[Ni1/3Co1/3Mn1/3]0.96Ti0.04O1.96F0.04 as cathode material for lithium-ion batteries," J. Alloys Compd., vol. 456, no. 1–2, pp. 344–347, 2008, DOI: 10.1016/j.jallcom.2007.02.074.

[32] R. K. Katiyar, R. Singhal, K. Asmar, R. Valentin, and R. S. Katiyar, "High voltage spinel cathode materials for high energy density and high rate capability Li-ion rechargeable batteries," J. Power Sources, vol. 194, no. 1, pp. 526–530, 2009, DOI: 10.1016/j.jpowsour.2009.05.017.

[33] B. Sambandam et al., "Investigation of Li-ion storage properties of earth-abundant B-Mn2V2O7prepared using facile green strategy," J. Power Sources, vol. 350, pp. 80–86, 2017, doi: 10.1016/j.jpowsour.2017.03.054.

[34] H. L. Zhang, R. Ren, and A. Jing, "Improvement of the electrochemical properties of LiMn2O 4 by doping rare-earth element Ce," Mater. Sci. Forum, vol. 686, pp. 716–719, 2011, DOI: 10.4028/www.scientific.net/MSF.686.716.

[35] V. Soundharrajan et al., "Aqueous Magnesium Zinc Hybrid Battery: An Advanced High-Voltage and High-Energy MgMn2O4 Cathode," ACS Energy Lett., vol. 3, no. 8, pp. 1998–2004, 2018, doi: 10.1021/acsenergylett.8b01105.

[36] M. H. Alfaruqi et al., "A high surface area tunnel-type α-MnO2 nanorod cathode by a simple solvent-free synthesis for rechargeable aqueous zinc-ion batteries," Chem. Phys. Lett., vol. 650, pp. 64–68, 2016, doi: 10.1016/j.cplett.2016.02.067.

[37] X. Wu et al., "Green-low-cost rechargeable aqueous zinc-ion batteries using hollow porous spinel ZnMn2O4 as the cathode material," J. Mater. Chem. A vol. 5, no. 34, pp. 17990–17997, 2017, DOI: 10.1039/c7ta00100b.

[38] N. H. Zainol, D. Hambali, Z. Osman, N. Kamarulzaman, and R. Rusdi, "Synthesis and characterization of Ti-doped MgMn 2 O 4 cathode material for magnesium ion batteries," Ionics (Kiel)., vol. 25, no. 1, pp. 133–139, 2019, DOI: 10.1007/s11581-018-2575-6.

[39] H. Li et al., "Carbon electrode with conductivity improvement using silver nanowires for high-performance supercapacitor," Appl. Phys. A Mater. Sci. Process., vol. 124, no. 11, pp. 1–8, 2018, doi: 10.1007/s00339-018-2182-4.

[40] M. Shang et al., "Nitrogen-doped carbon composite derived from ZIF-8/polyaniline@cellulose-derived carbon aerogel for high-performance symmetric supercapacitors," Carbohydr. Polym., vol. 262, no. January, p. 117966, 2021, doi: 10.1016/j.carbpol.2021.117966.

[41] N. M. Deghiedy, N. M. Yousif, H. M. Hosni, and M. R. Balboul, "Silver-modified electrodes based on amorphous MnO2/ carbon nanotube: Multicomponent approach to enhance the performance of supercapacitors," J. Phys. Chem. Solids, vol. 161, p. 110445, Feb. 2022, doi: 10.1016/J.JPCS.2021.110445.